Fast spectral source integration in black hole perturbation calculations

Seth Hopper,[1] Erik Forseth,[2] Thomas Osburn,[2] and Charles R. Evans[2]

[1]*School of Mathematical Sciences and Complex & Adaptive Systems Laboratory,*
University College Dublin, Belfield, Dublin 4, Ireland
[2]*Department of Physics and Astronomy, University of North Carolina, Chapel Hill, North Carolina 27599, USA*

This paper presents a new technique for achieving spectral accuracy and fast computational performance in a class of black hole perturbation and gravitational self-force calculations involving extreme mass ratios and generic orbits. Called *spectral source integration* (SSI), this method should see widespread future use in problems that entail (i) point-particle description of the small compact object, (ii) frequency domain decomposition, and (iii) use of the background eccentric geodesic motion. Frequency domain approaches are widely used in both perturbation theory flux-balance calculations and in local gravitational self-force calculations. Recent self-force calculations in Lorenz gauge, using the frequency domain and method of extended homogeneous solutions, have been able to accurately reach eccentricities as high as $e \simeq 0.7$. We show here SSI successfully applied to Lorenz gauge. In a double precision Lorenz gauge code, SSI enhances the accuracy of results and makes a factor of three improvement in the overall speed. The primary initial application of SSI–for us its *raison d'être*–is in an arbitrary precision *Mathematica* code that computes perturbations of eccentric orbits in the Regge-Wheeler gauge to extraordinarily high accuracy (e.g., 200 decimal places). These high accuracy eccentric orbit calculations would not be possible without the exponential convergence of SSI. We believe the method will extend to work for inspirals on Kerr, and will be the subject of a later publication. SSI borrows concepts from discrete-time signal processing and is used to calculate the mode normalization coefficients in perturbation theory via sums over modest numbers of points around an orbit. A variant of the idea is used to obtain spectral accuracy in solution of the geodesic orbital motion.

I. INTRODUCTION

Merging compact binaries are a promising source of detectable gravitational waves. Accurate theoretical models serve as templates to assist detection and will aid in estimating an event's physical parameters. Three complementary theoretical approaches exist [1] for computing relativistic binaries: numerical relativity [2, 3], post-Newtonian (PN) theory [4, 5], and gravitational self-force (GSF) and black hole perturbation (BHP) calculations [1, 6–9]. The effective-one-body (EOB) formalism, drawing calibration of its parameters from the above approaches, then provides a synthesis [10–15].

The GSF approach assumes the existence of, and exploits, a small ratio $q = \mu/M \ll 1$ between the component masses. The field and motion of the smaller body are calculated in a perturbation expansion in powers of q [16, 17]. Though restricted to small q, the GSF is valid throughout the strong field regime. GSF/BHP calculations are most relevant to potential future eLISA observations of extreme-mass-ratio inspirals (EMRIs) $q \simeq 10^{-7}$-10^{-4} [18] but might pertain to Advanced LIGO observations if there exists a fortuitous population of intermediate-mass-ratio inspirals (IMRIs) $q \simeq 10^{-3}$-10^{-2} [19, 20]. The dominant approach to the GSF treats the small body as a point mass [8], then calculates the metric perturbation and the local self-force using mode-sum regularization [21]. Calculations are done directly in the time domain (TD) [22–25] or via decomposition into Fourier-harmonic modes in the frequency domain (FD) [26–30]. Alternative means of calculating the GSF include effective source calculations [31–33] and direct Green function calculations [34–36].

The PN approach has no restriction on q but is most accurate for wide, low frequency orbits. Just as the GSF, PN, and NR approaches separately inform EOB, there has been considerable activity in recent years in making comparisons between GSF/BHP and PN theory [26, 37–39], including calculations at very high accuracies [40–43]. These high precision calculations, until recently all done for circular orbits, utilize the analytic function expansion formalism of Mano, Suzuki, and Takasugi (MST) [44] and make use of arbitrary precision coding.

Several of us were intrigued by the idea of extending MST calculations, and these comparisons, to include eccentric orbits. Initial results of that now successful effort will be described elsewhere [45], but the project led to the necessary development of the technique reported here. Modeling EMRIs with large eccentricities is essential, since astrophysical considerations suggest [18, 20] they have a distribution peaked about $e \simeq 0.7$ [46] as they enter eLISA's passband. Advanced LIGO inspirals are expected to have nearly circular orbits, but small eccentricity corrections may be important [47].

The spectral technique described here benefits FD calculations of the "geodesic self-force" (i.e., first-order perturbations derived using geodesics of the background geometry) in E/IMRIs with eccentric orbits. In eccentric-orbit FD calculations the Fourier transform spreads the influence of the point particle source across a range of radii. Mode by mode, the resulting source functions are integrated against a Green function over this radial li-

bration region, a procedure that has been followed for decades [48] for BHP problems. FD calculations of eccentric orbit GSF became feasible after Barack, Ori, and Sago [49] found the method of extended homogeneous solutions (EHS), thus allowing Fourier synthesis at the particle location without encountering Gibbs behavior. Originally demonstrated for scalar models [49] and early-on extended to master equations in the Regge-Wheeler-Zerilli (RWZ) formalism [27], EHS has recently been applied to coupled systems in Lorenz gauge [29, 30].

To those familiar with EHS, the new method can be outlined briefly here. See Secs. III and IV for details. Here we couch the discussion in terms of the RWZ case (Sec. III B), where EHS entails calculating arbitrarily normalized causal homogeneous solutions ($\hat{X}^-_{lmn}$, $\hat{X}^+_{lmn}$) and integrating them in product with stress-tensor projections over the source region. The result is a set of normalization coefficients $C^\pm_{lmn}$ that encode the orbital motion's imprint in the field perturbation. Then extended homogeneous solutions are assembled in the TD, and subsequently abutted at the instantaneous particle location.

The new technique provides a means of calculating the $C^\pm_{lmn}$ (or their equivalent in other gauges) with spectral accuracy. The integral for the normalization coefficients is typically manipulated [27, 49, 50] into a form like

$$C^\pm_{lmn} = \frac{1}{W_{lmn} T_r} \int_0^{T_r} \bar{E}^\pm_{lmn}(t) \, e^{in\Omega_r t} \, dt, \qquad (1.1)$$

where $\bar{E}^\pm_{lmn}(t)$ is a periodic function of the radial motion derived from spherical harmonic projection of the point source and integration over the $\hat{X}^\mp_{lmn}(r)$. Details are found in Sec. III but for the nonce it is enough to say that computing (1.1) is difficult to do with ODE or numerical quadrature integrators at high accuracies beyond double precision and is impossible to do at extraordinarily high accuracies like 100 or more decimal places. The new method, called *spectral source integration* (SSI), replaces the integral with a remarkably simple sum

$$C^\pm_{lmn} = \frac{1}{N W_{lmn}} \sum_{k=0}^{N-1} \bar{E}^\pm_{lmn}(t_k) \, e^{in\Omega_r t_k}, \qquad (1.2)$$

which involves merely sampling the source function $\bar{E}^\pm_{lmn}(t)$ at a modest number N of equally-spaced points around the closed radial motion. This sum converges *exponentially* with increases in N.

The FD approach with use of Fourier series (FS) has been a part of BHP theory for decades. The FS and normalization coefficients converge exponentially with n, allowing the FS to be truncated. The new method makes a crucial use of that standard approximation, recognizing that truncation of the FS representation (of e.g., a source term) generates a *bandlimited function*. That in turn invokes the machinery of the Nyquist-Shannon sampling theorem. The truncated FS can itself be replaced by discrete equally-spaced sampling of the TD function. Then, discrete sampling and periodicity allow a discrete

function of finite length N to serve as an accurate TD representation. Furthermore, the finite discrete function is dual to a discrete Fourier transform (DFT) spectrum, computable with an FFT. The DFT spectrum is an approximation, between its Nyquist frequencies, of the original FS spectrum, but can be made exponentially accurate with increases in N. It is then possible to replace integrals like (1.1) with finite sums like (1.2) and achieve spectral convergence there too. In essence, SSI provides a *completion* of the FD approach by bringing to bear concepts in discrete-time signal processing.

This paper shows application of SSI to FD BHP and geodesic GSF calculations of eccentric Schwarzschild E/IMRIs in both RWZ and Lorenz gauges. We also demonstrate in Sec. II that a related approach provides arbitrarily accurate solutions of the geodesic equations themselves. SSI may be applicable to Kerr BHP [6, 51, 52] and GSF calculations, the subject of an upcoming paper. In addition, SSI has the potential to benefit the Green function approach to GSF calculations [36].

This paper is organized as follows. Sec. II considers the orbital problem. In Sec. II A we review bound eccentric geodesic motion about a Schwarzschild black hole and set the notation. Sec. II C describes the spectral approach for integrating the orbit equations with geometric convergence, and shows numerical results. Appendix A gives a simple analytic calculation of the exponential fall-off in Fourier coefficients in part of the orbital problem. Next the SSI method is described in Sec. III through its application in the RWZ formalism to provide spectral solution of master equations. A brief review of how the RWZ problem is solved in the FD using EHS is given in Sec. III A. Then Sec. III B lays out the SSI method, the heart of this paper, and displays a set of numerical results. We discuss some related findings in the numerical analysis literature in Sec. III C. Having shown SSI applied to a single perturbation equation, we present next in Sec. IV its application in Lorenz gauge, demonstrating that the method allows systems of equations to be solved with spectral convergence. Our conclusions are drawn in Sec. V.

In this paper we set $G = c = 1$ and use the metric signature $+2$.

II. SPECTRAL INTEGRATION OF BOUND ORBITAL MOTION

The new method is first applied to solving the equations of bound geodesic motion. This proves to be a necessary first step to using SSI to solve the first-order perturbation equations when working at accuracies well beyond double precision. At double precision, it leads to a more efficient computation of the orbit. We consider geodesic motion about a Schwarzschild black hole in this paper. Application of SSI to general orbits about a Kerr black hole will be taken up in a subsequent paper. We begin with a brief review of the problem and notation.

A. Geodesic motion and the relativistic anomaly

We consider generic bound motion of a small mass μ, taken to be a point particle, around a Schwarzschild black hole of mass M in the test body (geodesic) limit $\mu/M \to 0$. Schwarzschild coordinates $x^\mu = (t, r, \theta, \varphi)$ are used, with the line element having the form

$$ds^2 = -f dt^2 + f^{-1} dr^2 + r^2 \left(d\theta^2 + \sin^2 \theta \, d\varphi^2\right), \quad (2.1)$$

where $f(r) = 1 - 2M/r$.

Let the worldline of the particle be described by the functions $x_p^\alpha(\tau) = [t_p(\tau), r_p(\tau), \theta_p(\tau), \varphi_p(\tau)]$ of proper time τ (or some other convenient curve parameter). Subscript p indicates location of the particle. The four-velocity is $u^\alpha = dx_p^\alpha/d\tau$. Without loss of generality the motion is confined to the equatorial plane, $\theta_p(\tau) = \pi/2$.

The orbit is parametrized in terms of the (dimensionless) semi-latus rectum p and the eccentricity e (see [48, 53]). These constants are related to the usual constant specific energy $\mathcal{E} = -u_t$ and specific angular momentum $\mathcal{L} = u_\varphi$. Additionally, pericentric $r_{\min}$ and apocentric $r_{\max}$ radii are introduced, which are related to p and e by the following equations

$$p = \frac{2 r_{\max} r_{\min}}{M(r_{\max} + r_{\min})}, \qquad e = \frac{r_{\max} - r_{\min}}{r_{\max} + r_{\min}}, \quad (2.2)$$

$$r_{\max} = \frac{pM}{1-e}, \qquad r_{\min} = \frac{pM}{1+e}. \quad (2.3)$$

Bound eccentric orbits satisfy $\mathcal{E} < 1$ and $\mathcal{L} > 2\sqrt{3}M$. These in turn imply $p \geq 6 + 2e$, with the boundary of stable orbits $p = 6 + 2e$ being the separatrix [48].

As is usual, τ is replaced as the curve parameter by Darwin's relativistic anomaly χ, in terms of which the radial position is given a Keplerian-appearing form [54]

$$r_p(\chi) = \frac{pM}{1 + e \cos \chi}. \quad (2.4)$$

The equations for the remaining functions take the form

$$\frac{dt_p}{d\chi} = \frac{r_p(\chi)^2}{M(p - 2 - 2e \cos \chi)} \sqrt{\frac{(p-2)^2 - 4e^2}{p - 6 - 2e \cos \chi}}, \quad (2.5)$$

$$\frac{d\tau_p}{d\chi} = \frac{M p^{3/2}}{(1 + e \cos \chi)^2} \sqrt{\frac{p - 3 - e^2}{p - 6 - 2e \cos \chi}}, \quad (2.6)$$

$$\frac{d\varphi_p}{d\chi} = \sqrt{\frac{p}{p - 6 - 2e \cos \chi}}. \quad (2.7)$$

The last equation, describing azimuthal motion, has an analytic solution

$$\varphi_p(\chi) = \sqrt{\frac{4p}{p - 6 - 2e}} \, F\left(\frac{\chi}{2} \,\middle|\, -\frac{4e}{p - 6 - 2e}\right), \quad (2.8)$$

where $F(x|m)$ is the incomplete elliptic integral of the first kind [55]. The other two equations are typically solved numerically.

To solve (2.5) and (2.6), each equation can be regarded as either a numerical quadrature or an initial value problem (IVP) [56]. Cutler, Kennefick, and Poisson [48] took the former approach and used Romberg's method. In the more complicated Kerr geodesic problem, Drasco and Hughes [51] initially solved for the motion using a numerical quadrature routine but later switched to use of a quasi-analytic approach developed by Fujita and Hikida [57]. (Indeed, this quasi-analytic method involving rapid evaluation of elliptic integrals stands as a third route to solution.) In more recent work [27, 29, 30, 53], Eqns. (2.5) and (2.6) have simply been integrated using Runge-Kutta routines. At double precision the distinction is trivial and errors in the orbit are of minimal concern. Recently, however, several of us have turned attention [45] to making extraordinarily high precision (e.g., 200 decimal place) BHP and GSF calculations for eccentric EMRIs using the MST formalism [44] (henceforth the MST code). It proved necessary to develop a new means of efficiently calculating the orbit to arbitrary precision, as well as doing the same for the perturbation source integration (Secs. III B and IV B).

The MST code is written in *Mathematica* to make use of its arbitrary precision functionality. Initially, we used its NDSolve function to compute orbits but found such integrations became prohibitively expensive for errors of order $\lesssim 10^{-40}$. The alternative approach we found turns out to be a simple application of the SSI concepts. In fact, the arguments laid out in the next two subsections are key to understanding the SSI development. Shortly, we will discuss solving (2.5) to obtain $t_p(\chi)$ (integration of (2.6) follows in like fashion). But first we address some general considerations.

B. Spectral integration: general considerations

Let $dI/d\chi = g(\chi)$ with $g(\chi)$ (the source) being both a periodic and a smooth function. We are interested in integrating g to find $I(\chi)$. We can assume $g(\chi)$ is complex, but in orbital motion applications the functions will be real. The periodicity of g suggests utilizing a FS expansion and then calculating the integral for $I(\chi)$ term by term. At first glance this approach is not very helpful since, even if we truncate the FS, the expression for $I(\chi)$ would require computing a large number of definite integrals numerically for the FS coefficients. Fortunately, the smoothness of $g(\chi)$ helps in several ways. In many cases, the FS amplitudes $\tilde{\mathcal{G}}_n$ will fall in magnitude exponentially (shown numerically for orbital motion presently; see also Appendix A). Even in calculations with hundreds of decimal places of accuracy, the FS can then be truncated to a modest number of terms. At whatever adopted level of accuracy, replacing $g(\chi)$ with a truncated FS introduces an approximation that is *bandlimited*.

We then recall that bandlimited signals play a key role in the Nyquist-Shannon sampling theorem: a function that contains only frequencies f with $|f| \leq B$ is com-

pletely determined by its discrete (equally-spaced) samples (in this case in χ) occurring at the Nyquist rate $2B$ (i.e., with spacing $\Delta\chi = \frac{1}{2}B^{-1}$). If we combine discrete sampling with the periodicity of radial motion, then only a finite total number N of samples in χ need be considered. We replace $g(\chi)$ again–this time with its finite sampling $g_k = g(\chi_k) = g(k\Delta\chi)$, where $k = 0, \ldots, N-1$. This new representation of the source has its own DFT spectrum $\mathcal{G}_n$ (with $n = -N/2, \ldots, N/2 - 1$), which can be computed with the FFT algorithm [56]. In contrast to the FS spectrum $\tilde{\mathcal{G}}_n$, the DFT spectrum $\mathcal{G}_n$ exhibits a periodicity of its own, $\mathcal{G}_{n+jN} = \mathcal{G}_n$, for arbitrary integer j. However, aliasing can be avoided if the DFT spectrum is only used at the N frequencies within its Nyquist bounds. Then for an accuracy goal that is sufficiently high (i.e., high enough N, found iteratively), the DFT spectrum $\mathcal{G}_n$ is virtually indistinguishable from the FS spectrum $\tilde{\mathcal{G}}_n$. Using the DFT representation, it is then possible to compute $g(\chi)$ at any location either via Fourier interpolation or using the Whittaker cardinal function [58] on the circle (i.e., convolution with the Dirichlet kernel). Furthermore, the source can be integrated or differentiated term by term to accuracies comparable to the initial goal.

To summarize:

- The (perhaps complex) function $g(\chi)$ is periodic and C^∞.

- It can be represented as a FS with spectrum $\tilde{\mathcal{G}}_n$ with $n \to \pm\infty$.

- The FS spectrum can be truncated to some $n_{\min} \leq n \leq n_{\max}$ subject to an accuracy goal.

- The approximate but very accurate truncated FS is a bandlimited function.

- The Nyquist-Shannon sampling theorem implies the truncated FS representation can itself be replaced in the TD with discrete sampling.

- Sampling plus periodicity implies a discrete representation of finite length N.

- Finite sampling representation in the TD implies one-to-one correspondence via the DFT with a FD periodic spectrum $\mathcal{G}_n$.

- The DFT spectrum within the Nyquist range approximates well the original FS spectrum if N is sufficiently large, allowing $\tilde{\mathcal{G}}_n \to \mathcal{G}_n$.

- The DFT representation in the TD can be integrated and interpolated to spectral accuracy.

C. Spectral solution of the orbital motion

In practice, the orbit equations (2.5) and (2.6) have source functions that are real and even. Hence we can
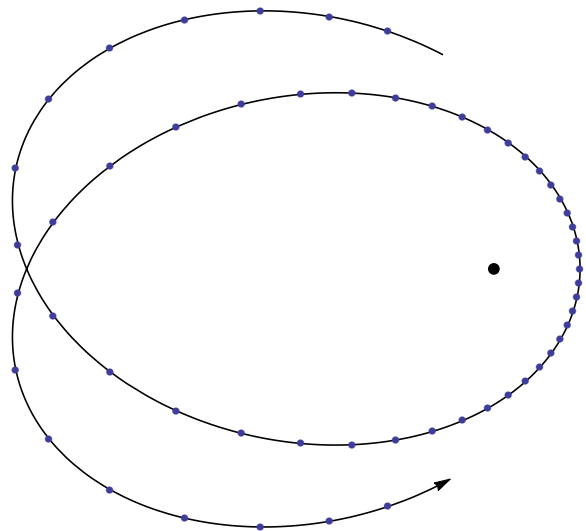

FIG. 1.   Equally spaced in χ sampling of $p = 50$, $e = 0.7$ orbit. The complete orbit is split into $N = 42$ samples ($\Delta\chi = 0.1496$) and spectral integration requires only $\mathcal{N} = 22$ points between $\chi = 0$ and $\chi = \pi$ (inclusive) to achieve double precision accuracy. The values of $dt_p/d\chi$ need only be calculated at the indicated points to provide double precision integration and interpolation anywhere on the orbit.

represent them with a discrete cosine transform (DCT) [59]. In turn the integral for $t_p(\chi)$ (for example) will be represented by a discrete sine transform (DST), with an additional term linear in χ. Furthermore, the orbital source functions are not only periodic but have reflection symmetries across both periapsis ($\chi = 0$) and apapsis ($\chi = \pi$). These symmetries narrow the form that the DCT can take to be either type I or II [60]. We utilize the type I (referred to as DCT-I) algorithm with unitary normalization (making the DCT-I its own inverse).

In the general discussion above, we imagined dividing the entire orbit into N intervals with $\Delta\chi = 2\pi/N$. For the DCT-I, this spacing is maintained and (assuming N is even) the half orbit from $\chi = 0$ to $\chi = \pi$ is split into $N/2$ intervals. The DCT-I utilizes $\mathcal{N} = N/2 + 1$ sample points by including the end points at both $\chi = 0$ and $\chi = \pi$. In terms of the number of samples the domain is split into $\mathcal{N} - 1$ intervals. The locations of the samples are

$$\chi_k \equiv \frac{k\pi}{\mathcal{N} - 1}, \qquad k \in 0, 1, \ldots, \mathcal{N} - 1. \qquad (2.9)$$

Then at the $\mathcal{N}$ points we denote the samples of the source function as $g_k = g(\chi_k)$. The (real) Fourier coefficients are given by

$$\mathcal{G}_n = \sqrt{\frac{2}{\mathcal{N} - 1}} \left[\frac{1}{2}g_0 + \frac{1}{2}(-1)^n g_{\mathcal{N}-1} \qquad (2.10) \right.$$
$$\left. + \sum_{k=1}^{\mathcal{N}-2} g_k \cos\left(n\chi_k\right) \right].$$
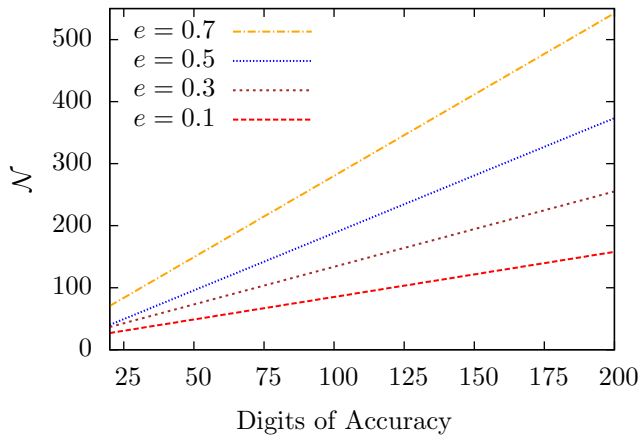
FIG. 2. Number of sample points $\mathcal{N}$ between $\chi = 0$ and $\chi = \pi$ needed to represent $dt_p/d\chi = g(\chi)$ to a prescribed accuracy. The ratio of magnitudes of the smallest to largest Fourier coefficients of $g(\chi)$ gives an estimate of the relative accuracy. The linear scaling of $\mathcal{N}$ versus digits of accuracy indicates geometric fall-off in the spectral components of $g(\chi)$. Away from the separatrix this relation is largely independent of p.
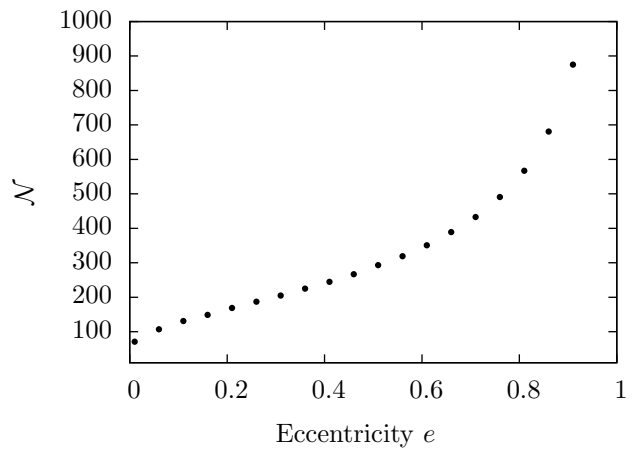
FIG. 3. Number of sample points $\mathcal{N}$ between $\chi = 0$ and $\chi = \pi$ needed to represent $dt_p/d\chi = g(\chi)$ as a function of eccentricity e at fixed accuracy of 150 decimal places. Of course as the eccentricity approaches unity and the radial period becomes infinite, so too does the number of needed samples. Still, for any astrophysically relevant orbit, we can sample the orbit to impressive accuracy with a modest number of points.

Like the more general DFT, this expression is exactly invertible and we can recover the original samples in the χ-domain

$$g_k = \sqrt{\frac{2}{\mathcal{N}-1}}\left[\frac{1}{2}\mathcal{G}_0 + \frac{1}{2}(-1)^k \mathcal{G}_{\mathcal{N}-1} \right. \tag{2.11}$$
$$\left. + \sum_{n=1}^{\mathcal{N}-2} \mathcal{G}_n \cos(n\chi_k) \right].$$

We can then use the spectral amplitudes to provide a Fourier interpolation to arbitrary χ

$$g(\chi) = \sqrt{\frac{2}{\mathcal{N}-1}}\left[\frac{1}{2}\mathcal{G}_0 + \frac{1}{2}\mathcal{G}_{\mathcal{N}-1}\cos[(\mathcal{N}-1)\chi] \right.$$
$$\left. + \sum_{n=1}^{\mathcal{N}-2} \mathcal{G}_n \cos(n\chi) \right]. \tag{2.12}$$

Integrating Eqn. (2.12) yields the sine expansion for the time

$$t_p(\chi) = \sqrt{\frac{2}{\mathcal{N}-1}}\left[\frac{1}{2}\mathcal{G}_0\chi + \frac{1}{2}\mathcal{G}_{\mathcal{N}-1}\frac{\sin[(\mathcal{N}-1)\chi]}{(\mathcal{N}-1)} \right.$$
$$\left. + \sum_{n=1}^{\mathcal{N}-2} \frac{1}{n}\mathcal{G}_n \sin(n\chi) \right]. \tag{2.13}$$

Having found $t_p(\chi)$ we can obtain the radial period T_r from the leading Fourier amplitude $\mathcal{G}_0$

$$T_r = \sqrt{\frac{2}{\mathcal{N}-1}}\pi\mathcal{G}_0. \tag{2.14}$$

Then, with T_r in hand, the fundamental frequencies can be computed

$$\Omega_r = \frac{2\pi}{T_r}, \qquad \Omega_\varphi = \frac{\varphi_p(2\pi)}{T_r}. \tag{2.15}$$

From a practical perspective, the DCT-I can be computed with $\mathcal{O}(\mathcal{N}\ln\mathcal{N})$ speed using either the FourierDCT function in *Mathematica* or the FFTW routine in C coding. Fig. 1 provides a picture of how efficient this method is. For this orbit we need only $\mathcal{N} = 22$ samples to achieve double precision accuracy in the orbit integration. In fact, all we need know are the source functions at the indicated points and we can interpolate to double precision accuracy anywhere in between. From a practical standpoint, we guess a value of $\mathcal{N}$ and estimate the error by computing the ratio of the smallest to largest Fourier coefficients $|\mathcal{G}_{\mathcal{N}-1}/\mathcal{G}_0|$. If that ratio fails to meet our prescribed accuracy goal, we simply increase $\mathcal{N}$ and repeat the procedure. Given that the DCT is so fast to compute, we are able to solve the orbit equations to hundreds of digits of accuracy within a few seconds. Fig. 2 shows how remarkable and modest the scaling is in the number of required sample points $\mathcal{N}$ as a function of prescribed accuracy. Fig. 3 shows how the number of needed sample points grows with increasing eccentricity (given a fixed accuracy goal). Even at very high eccentricities, $e \approx 0.9$, the number of samples is quite reasonable. Thus, with this approach the integration of the orbit becomes a trivial cost, even for astrophysically interesting eccentricities ($e \simeq 0.7$) and high accuracy (MST code) applications.

III. SPECTRAL SOURCE INTEGRATION IN THE RWZ FORMALISM

One of the principal goals of this paper is to describe our new means of applying spectral techniques (i.e., SSI) to integrate the source problem in black hole perturbation theory to high accuracy. In this section we show the simplest application of SSI, namely solution of master equations in the Regge-Wheeler-Zerilli (RWZ) formalism for generic orbits. Before detailing the SSI technique in Sec. III B, we first briefly review the now standard way [27] of solving master equations using FD decomposition and the method of extended homogeneous solutions (EHS) [49], and in the process set the notation.

A. The RWZ formalism and EHS method

We begin with a RWZ master equation in the TD

$$\left(-\frac{\partial^2}{\partial t^2} + \frac{\partial^2}{\partial r_*^2} - V_l(r)\right)\Psi_{lm}(t,r) = S_{lm}(t,r), \quad (3.1)$$

where $r_* = r + 2M\ln(r/2M - 1)$ is the usual tortoise coordinate. Here $V_l(r)$ is either the Zerilli potential ($l + m$ even) or the Regge-Wheeler potential ($l + m$ odd). The source contains terms proportional to the Dirac delta function and its first derivative

$$S_{lm}(t,r) = G_{lm}(t)\,\delta[r - r_p(t)] \\ + F_{lm}(t)\,\delta'[r - r_p(t)]. \quad (3.2)$$

The time dependent functions $G_{lm}(t)$ and $F_{lm}(t)$ arise from tensor spherical harmonic decomposition [27] of the stress-energy tensor of the point mass and enforcement of the delta function constraints $r \rightarrow r_p(t)$ and $\varphi \rightarrow \varphi_p(t)$. Like the potential, their form depends upon parity. For $l + m$ even we use the Zerilli-Moncrief source, and for $l + m$ odd we use the Cunningham-Price-Moncrief source (see [27] for details).

As explained in Sec. II, the eccentric motion of the source is characterized by two fundamental frequencies, Ω_φ and Ω_r. As such, we can represent the master function and the source as Fourier series

$$\Psi_{lm}(t,r) = \sum_{n=-\infty}^{\infty} X_{lmn}(r)\,e^{-i\omega t}, \quad (3.3)$$

$$S_{lm}(t,r) = \sum_{n=-\infty}^{\infty} Z_{lmn}(r)\,e^{-i\omega t}, \quad (3.4)$$

with the mode frequencies being functions of both fundamentals

$$\omega = \omega_{mn} \equiv m\Omega_\varphi + n\Omega_r, \qquad m,n \in \mathbb{Z}. \quad (3.5)$$

The series coefficients are formally found by integrating the TD master functions over one radial period

$$X_{lmn}(r) \equiv \frac{1}{T_r}\int_0^{T_r} dt\,\Psi_{lm}(t,r)\,e^{i\omega t}, \quad (3.6)$$

$$Z_{lmn}(r) \equiv \frac{1}{T_r}\int_0^{T_r} dt\,S_{lm}(t,r)\,e^{i\omega t}. \quad (3.7)$$

The master equation then takes on the following FD form

$$\left(\frac{d^2}{dr_*^2} + \omega^2 - V_l(r)\right)X_{lmn}(r) = Z_{lmn}(r). \quad (3.8)$$

(Throughout Sec. III we do *not* suppress any of the mode labels, though for all intents and purposes l and m can be regarded as fixed and arbitrary.)

An essential element in solving (3.1) is to obtain independent homogeneous solutions to (3.8), either through numerical integration (after setting causal boundary conditions at $r_* \rightarrow \infty$ and $r_* \rightarrow -\infty$) or through use of analytic function (MST) expansions [61]. We denote these unnormalized solutions as $\hat{X}_{lmn}^\pm(r)$, where

$$\hat{X}_{lmn}^+(r_* \rightarrow +\infty) \sim e^{i\omega r_*}, \quad (3.9)$$

$$\hat{X}_{lmn}^-(r_* \rightarrow -\infty) \sim e^{-i\omega r_*}. \quad (3.10)$$

A Green function is formed from these two linearly independent solutions and integrated over the source function $Z_{lmn}(r)$ to obtain the particular solution of (3.8)

$$X_{lmn}(r) = c_{lmn}^+(r)\,\hat{X}_{lmn}^+(r) + c_{lmn}^-(r)\,\hat{X}_{lmn}^-(r), \quad (3.11)$$

where the normalization functions in the source region are given by the integrals

$$c_{lmn}^+(r) = \frac{1}{W_{lmn}}\int_{r_{\min}}^{r} \frac{dr'}{f(r')}\hat{X}_{lmn}^-(r')\,Z_{lmn}(r'), \\ c_{lmn}^-(r) = \frac{1}{W_{lmn}}\int_{r}^{r_{\max}} \frac{dr'}{f(r')}\hat{X}_{lmn}^+(r')\,Z_{lmn}(r'). \quad (3.12)$$

Here W_{lmn} is the Wronskian

$$W_{lmn} = f(r)\left(\hat{X}_{lmn}^- \frac{d\hat{X}_{lmn}^+}{dr} - \hat{X}_{lmn}^+ \frac{d\hat{X}_{lmn}^-}{dr}\right). \quad (3.13)$$

While the expression in Eqn. (3.11) is indeed a solution to Eqn. (3.8), it is not ideal. The singular nature of the TD source (3.2) results in Gibbs behavior in the Fourier synthesis (3.3) of Ψ_{lm} at and near the particle location, leading to slow algebraic convergence. Exponential convergence can be restored by using the method of EHS, originally developed by Barack, Ori and Sago [49].

The first step in EHS is to extend the limits of integration in (3.12) to include the full source region and obtain the normalization coefficients

$$C_{lmn}^\pm = \frac{1}{W_{lmn}}\int_{r_{\min}}^{r_{\max}} dr\,\frac{\hat{X}_{lmn}^\mp(r)Z_{lmn}(r)}{f(r)}. \quad (3.14)$$

These complex constants are in turn used to normalize the individual mode functions

$$X_{lmn}^{\pm}(r) = C_{lmn}^{\pm} \hat{X}_{lmn}^{\pm}(r), \qquad (3.15)$$

producing the FD EHS of Eqn. (3.8). Collectively, these normalized modes encode all the information about the source motion and are used to then define the TD EHS

$$\Psi_{lm}^{\pm}(t,r) \equiv \sum_n X_{lmn}^{\pm}(r)\, e^{-i\omega t}. \qquad (3.16)$$

As the FD EHS are each C^{∞}, these Fourier sums converge exponentially for all $r > 2M$. The sums are formally infinite in number, but in practice they are truncated once a specified accuracy is reached. The desired particular TD solution to Eqn. (3.1) is then obtained by joining the outer and inner TD EHS:

$$\Psi_{lm}(t,r) = \Psi_{lm}^{+}\theta\left[r - r_p(t)\right] + \Psi_{lm}^{-}\theta\left[r_p(t) - r\right]. \quad (3.17)$$

This weak solution can be computed everywhere, including the particle location, and it allows the metric and local gravitational self-force to be accurately determined [27].

There remains the practical issue of computing the $C_{lmn}^{\pm}$. For the RWZ problem, the source $Z_{lmn}(r)$ in Eqn. (3.14) is poorly behaved at the turning points because of the presence of the δ' term in (3.2) [27]. It was shown in that paper that the problem could be circumvented by reversing the order of integration (see related examples in [49, 50]). To see this, substitute the Fourier transform integral for $Z_{lmn}(r)$ into (3.14)

$$C_{lmn}^{\pm} = \frac{1}{W_{lmn}T_r} \int_{r_{\min}}^{r_{\max}} dr\, \frac{\hat{X}_{lmn}^{\mp}(r)}{f(r)} \qquad (3.18)$$
$$\times \int_0^{T_r} dt\, S_{lm}(t,r) e^{i\omega t}.$$

Then substitute for the TD source $S_{lm}(t,r)$ its singular form (3.2), exchange the order of integration, and integrate in r over the delta function terms. What remains of the calculation of $C_{lmn}^{\pm}$ is an integral over time

$$C_{lmn}^{\pm} = \frac{1}{W_{lmn}T_r} \int_0^{T_r} \left[\frac{1}{f_p} \hat{X}_{lmn}^{\mp} G_{lm} \right. \qquad (3.19)$$
$$\left. + \left(\frac{2M}{r_p^2 f_p^2} \hat{X}_{lmn}^{\mp} - \frac{1}{f_p}\frac{d\hat{X}_{lmn}^{\mp}}{dr} \right) F_{lm} \right] e^{i\omega t}\, dt.$$

The integrand is composed of obvious functions of time, such as $G_{lm}(t)$ and $F_{lm}(t)$. However, all of the other terms inside the square braces are now also functions of time, since the delta function maps $r \rightarrow r_p(t)$ [e.g., $f_p \equiv f(r_p(t))$, $\hat{X}_{lmn}^{\mp}(r) \rightarrow \hat{X}_{lmn}^{\mp}(r_p(t))$].

In summary, the RWZ BHP problem is solved by computing, for a sufficient range of l, m, and n, the inner and outer mode functions $\hat{X}_{lmn}^{\pm}(r)$ (by ODE integration or analytic function expansion) and computing the integrals (3.19) for the normalization coefficients $C_{lmn}^{\pm}$ (using either IVP ODE integration [27] or a numerical quadrature routine [50]).

B. SSI for the normalization coefficients

SSI is a new modification in the way the normalization coefficients $C_{lmn}^{\pm}$ are calculated. The key first step in developing SSI was actually the reversal in the order of integration described immediately above. The second essential step involves recognizing the periodic nature of the integrand in (3.19). The functions $F_{lm}(t)$ and $G_{lm}(t)$, which contribute to the source S_{lm}, have complex time dependence because of the biperiodic motion and (typically) incommensurate frequencies Ω_r and Ω_{φ}. The motion in φ can be split into

$$\varphi_p(t) = \Omega_{\varphi}t + \Delta\varphi(t), \qquad (3.20)$$

where the mean azimuthal advance is modulated by $\Delta\varphi(t)$, which is periodic in the radial motion. This $\varphi_p(t)$ enters source terms only through the spherical harmonic factor $e^{-im\varphi_p(t)}$, which factors into: $e^{-im\Omega_{\varphi}t}\, e^{-im\Delta\varphi(t)}$. It is the mean azimuthal phase advance, at angular rate Ω_{φ}, that makes source terms biperiodic. We can, however, define functions $\bar{G}_{lm}$ and $\bar{F}_{lm}$ via

$$\begin{aligned} \bar{G}_{lm}(t) &\equiv G_{lm}(t)\, e^{im\Omega_{\varphi}t}, \\ \bar{F}_{lm}(t) &\equiv F_{lm}(t)\, e^{im\Omega_{\varphi}t}, \end{aligned} \qquad (3.21)$$

that are strictly T_r-periodic. Returning to Eqn. (3.19), we see that the factor, $e^{-im\Omega_{\varphi}t}$, responsible for biperiodicity, cancels with a corresponding factor from the Fourier transform kernel. We can replace the integral with

$$C_{lmn}^{\pm} = \frac{1}{W_{lmn}T_r} \int_0^{T_r} \bar{E}_{lmn}^{\pm}(t)\, e^{in\Omega_r t}\, dt. \qquad (3.22)$$

where $\bar{E}_{lmn}^{\pm}(t)$ are strictly T_r-periodic functions

$$\bar{E}_{lmn}^{\pm}(t) \equiv \frac{1}{f_p} \hat{X}_{lmn}^{\mp} \bar{G}_{lm} \qquad (3.23)$$
$$+ \left(\frac{2M}{r_p^2 f_p^2} \hat{X}_{lmn}^{\mp} - \frac{1}{f_p}\frac{d\hat{X}_{lmn}^{\mp}}{dr} \right) \bar{F}_{lm}.$$

The third, and most important, step toward SSI harks back to our earlier discussion in Sec. II C of spectrally integrating the orbit equations. There we showed that due to the C^{∞} smoothness of (for example) $dt_p/d\chi = g(\chi)$ we could replace $g(\chi)$ with an equally-spaced sampling $g_k = g(k\Delta\chi)$ of modest total number of samples N and achieve high-accuracy interpolation and integration. For source integration, the equivalent step (to be justified momentarily) is to replace (3.22) with

$$C_{lmn}^{\pm} = \frac{1}{N W_{lmn}} \sum_{k=0}^{N-1} \bar{E}_{lmn}^{\pm}(t_k)\, e^{in\Omega_r t_k}, \qquad (3.24)$$

where the time samples are $t_k = kT_r/N$, with $k = 0, \ldots, N-1$. *This remarkably simple sum is the heart of SSI.* By replacing the integral in (3.22) with the sum

in (3.24), we avoid ODE integration and the calculation of the normalization coefficients is vastly sped up, opening the door to much higher accuracy applications [45].

What makes SSI work? Before we examine how well SSI performs, we first justify (3.24) as an appropriate replacement for (3.22). The argument starts by noting the expected smoothness of the functions $\bar{E}_{lmn}^{\pm}(t)$ that enter (3.22). The contributing elements $\bar{F}_{lm}(t)$ and $\bar{G}_{lm}(t)$ are smooth C^{∞} functions of the orbital motion. Similarly, the modes $\hat{X}_{lmn}^{\mp}(r)$ are smooth functions of r, and hence become smooth functions of time under the replacement $r \to r_p(t)$. Thus, for every lmn, the integrand in (3.22) is smooth and periodic. These properties suggest, just as they did in Sec. II B, use of FS expansion. Indeed, the integral in Eqn. (3.22) looks like, under a cursory glance, the calculation of a set of FS coefficients. However, it is clear that $C_{lmn}^{\pm}$ is not a spectrum of coefficients (in n) derived from a single function of time, but is instead calculated from a whole set (in n) of TD functions $\bar{E}_{lmn}^{\pm}(t)$.

Nevertheless, the Fourier series can be put to investigative use and we introduce one for each $\bar{E}_{lmn}^{\pm}(t)$:

$$\bar{E}_{lmn}^{\pm}(t) = \sum_{n'=-\infty}^{\infty} \tilde{\mathcal{E}}_{lmnn'}^{\pm} \, e^{-in'\Omega_r t}, \qquad (3.25)$$

with the coefficients given by

$$\tilde{\mathcal{E}}_{lmnn'}^{\pm} = \frac{1}{T_r} \int_0^{T_r} dt \, \bar{E}_{lmn}^{\pm}(t) \, e^{in'\Omega_r t}. \qquad (3.26)$$

If (3.25) is substituted in (3.22), and sum and integral are exchanged, we find that the normalization coefficients

$$C_{lmn}^{\pm} = \frac{1}{W_{lmn}} \tilde{\mathcal{E}}_{lmnn}^{\pm} \quad, \qquad (3.27)$$

are proportional to the diagonal elements ($n = n'$) of the superset (over n and n') of FS coefficients $\tilde{\mathcal{E}}_{lmnn'}^{\pm}$. The result is understandable: the integral in (3.22) simply picks out the nth harmonic in the nth function $\bar{E}_{lmn}^{\pm}(t)$.

To complete the argument, we may assume (and numerically verify) that the smoothness of a source function $\bar{E}_{lmn}^{\pm}(t)$ implies a rapidly falling (likely geometric) spectrum for $\tilde{\mathcal{E}}_{lmnn'}^{\pm}$ as $n' \to \pm\infty$. As we argued in Sec. II B, for any given accuracy goal, this implies the spectrum can be truncated at some sufficiently negative and positive values of n'. Truncation, in turn, means that we have replaced the original source function with a bandlimited approximation. Bandlimiting then argues for replacing the source function (yet again), this time with a set of discrete, equally-spaced samples $\bar{E}_{lmn}^{\pm}(t_k)$. Because the source function is periodic, the discrete sampling is finite in number (say N). We can then use the DFT to relate the discrete sampling representation of the source to a discrete, finite spectrum (and vice versa)

$$\bar{E}_{lmn}^{\pm}(t_k) = \sum_{n'=0}^{N-1} \mathcal{E}_{lmnn'}^{\pm} \, e^{-in'\Omega_r t_k}, \qquad (3.28)$$

$$\mathcal{E}_{lmnn'}^{\pm} = \frac{1}{N} \sum_{k=0}^{N-1} \bar{E}_{lmn}^{\pm}(t_k) \, e^{in'\Omega_r t_k}. \qquad (3.29)$$

The DFT spectrum $\mathcal{E}_{lmnn'}^{\pm}$ is distinct from the FS spectrum $\tilde{\mathcal{E}}_{lmnn'}^{\pm}$, and the former will display periodicity in the FD, $\mathcal{E}_{lmn,n'+jN}^{\pm} = \mathcal{E}_{lmnn'}^{\pm}$. However, for sufficiently large N and between the negative and positive Nyquist frequencies, the two spectra can be made nearly indistinguishable. If we then set $n' = n$, replace $\tilde{\mathcal{E}}_{lmnn}^{\pm}$ in (3.27) with the DFT spectral component $\mathcal{E}_{lmnn}^{\pm}$, and substitute into the same equation the DFT relation (3.29), we have derived our SSI formula Eqn. (3.24).

We can provide a summary of this discussion, and the derivation, through a sequence of replacements:

$$C_{lmn}^{\pm} = \frac{1}{W_{lmn}T_r} \int_0^{T_r} dt \, \bar{E}_{lmn}^{\pm}(t) \, e^{in\Omega_r t} \qquad (3.30)$$

$$= \frac{1}{W_{lmn}T_r} \int_0^{T_r} dt \, e^{in\Omega_r t} \sum_{n'=-\infty}^{\infty} \tilde{\mathcal{E}}_{lmnn'}^{\pm} \, e^{-in'\Omega_r t}$$

$$\simeq \frac{1}{W_{lmn}T_r} \int_0^{T_r} dt \, e^{in\Omega_r t} \sum_{n'=n'_{\min}}^{n'_{\max}} \tilde{\mathcal{E}}_{lmnn'}^{\pm} \, e^{-in'\Omega_r t}$$

$$\simeq \frac{1}{W_{lmn}T_r} \int_0^{T_r} dt \, e^{in\Omega_r t} \sum_{n'=n'_{\min}}^{n'_{\max}} \mathcal{E}_{lmnn'}^{\pm} \, e^{-in'\Omega_r t}$$

$$= \frac{1}{W_{lmn}T_r} \int_0^{T_r} dt \, e^{in\Omega_r t} \sum_{n'=n'_{\min}}^{n'_{\max}} e^{-in'\Omega_r t}$$

$$\times \frac{1}{N} \sum_{k=0}^{N-1} \bar{E}_{lmn}^{\pm}(t_k) \, e^{in'\Omega_r t_k}$$

$$= \frac{1}{NW_{lmn}} \sum_{n'=n'_{\min}}^{n'_{\max}} \sum_{k=0}^{N-1} \bar{E}_{lmn}^{\pm}(t_k) \, e^{in'\Omega_r t_k} \, \delta_{nn'}$$

$$= \frac{1}{NW_{lmn}} \sum_{k=0}^{N-1} \bar{E}_{lmn}^{\pm}(t_k) \, e^{in\Omega_r t_k}.$$

The two approximate (but typically spectrally accurate) steps are indicated.

What is involved in practical use of SSI? Another way of asking this question is: if we make N discrete samples of each source function and sum them in (3.24), for which and how many n's should we compute $C_{lmn}^{\pm}$? We do not presently have an exact answer, but we have an effective, practical procedure. To see the issue, consider Fig. 4. There we show gravitational wave energy fluxes per harmonic n at $r = \infty$ for the $l = 2$, $m = 2$ mode (essentially proportional to $|C_{22n}^{+}|^2$). We might expect, for a given N, to begin near $n = 0$ and see a spectrum that descends on either side until hitting a Nyquist point (at about $n = \pm N/2$). That is roughly, but not exactly, what is observed. The problem is that $C_{lmn}^{\pm}$ is not, as a function of n, a DFT spectrum. If we consider (3.27), clearly the Wronskian W_{lmn} should not be expected to
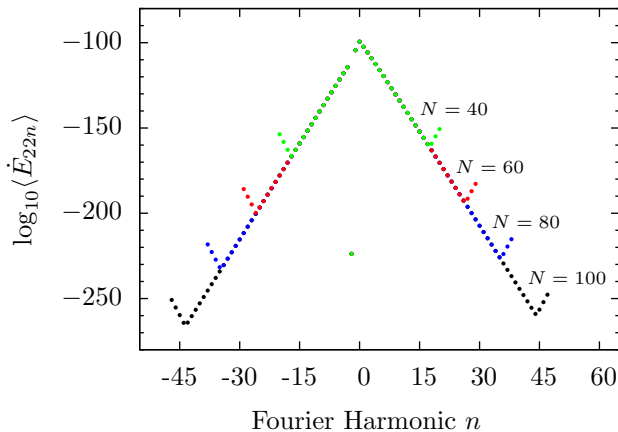
FIG. 4. Aliasing effect from oversampling SSI in the FD. Shown here are energy flux data from an orbit with $p = 10^{20}$ and $e = 0.01$ for modes with $l = 2$, $m = 2$. The energy flux from successive n modes falls off exponentially when computed away from the peak harmonic. Note that one harmonic $(n = -m = -2)$ is nearly static, which decreases its flux by more than 100 orders of magnitude. As higher positive and negative n are computed, the fluxes reach Nyquist-like notches and oversampling in n beyond those points leads to increases in flux similar to aliasing. The locations of the minima scale with but are not equal to $\pm N/2$.

display a periodicity in n. Even the DFT spectra, while having the periodicity in n', $\mathcal{E}^{\pm}_{lmn,n'+jN} = \mathcal{E}^{\pm}_{lmnn'}$, will not have a periodicity in the diagonal elements $\mathcal{E}^{\pm}_{lmnn}$ as a function of n. Nevertheless, if we sample $C^{\pm}_{lmn}$ in n for $|n| \gtrsim N/2$ we observe a succession of Nyquist-like notches and peaks, similar to aliasing in the DFT but without exact periodicity. From a practical standpoint, we compute and use the spectrum in n down to the first Nyquist-like notch on each side and calculate no further. The code marches forward on each side, finds the minima, and discards contributions beyond those points.

Fig. 4 shows this aliasing phenomenon. There we deliberately compute and display energy fluxes for a few harmonics beyond the first Nyquist notch on each side of the central maximum. We show the same fluxes computed with four different spectral resolutions. The exponential fall in the spectrum is evident. These calculations were made possible not only by use of SSI but also *Mathematica's* arbitrary precision arithmetic. As N becomes larger, we approach the FS, or continuum, limit. It is clear from the vantage point of high resolution that the best thing to do at lower resolution is halt the mode calculations at the Nyquist notches. This assumption is borne out by considering Fig. 5. This figure displays the differences in fluxes between those computed at resolutions of $N = 40, 60, 80$ and those found with $N = 100$. The error in the discrete representation is well bounded in the region between the first Nyquist points by the maximum error at one of the notches.

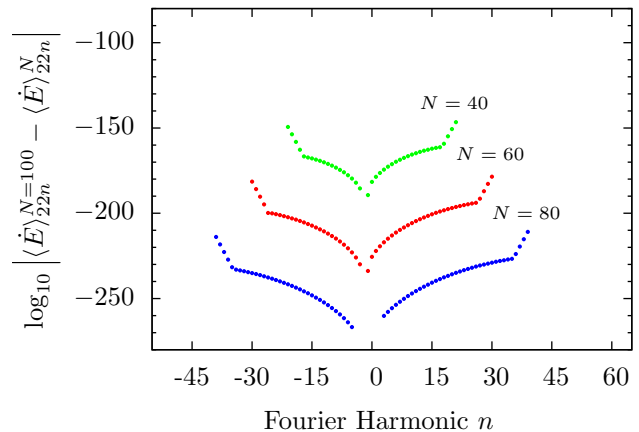Operating at high accuracy (e.g., 200 decimal places),

FIG. 5. SSI at high accuracy. Absolute differences (errors) are shown in self-convergence tests. The same data found in Fig. 4 are used to compute differences (per harmonic) in the fluxes between the three lower resolutions and the highest $(N = 100)$ resolution. For each of the three lower resolutions $(N = 40, 60, 80)$ the errors are well bounded by the accuracy criteria set by errors at the Nyquist notches.

the MST code makes a prediction of how large N needs to be in order that the Nyquist notches lie (just) below the specified error level. We have observed that adequate sampling for SSI is always sufficient for comparably accurate orbit integration. The prediction for N is tested and if mode fluxes do not reach the error level at the Nyquist notches, then a new value of N is chosen and the calculation is repeated. In the MST code, the now vastly reduced number of function evaluations can still be expensive if N is set too generously. It is important to note that the key formula for SSI, Eqn. (3.24) (or more properly (3.31)–see below), is an $\mathcal{O}(N^2)$ procedure, and so it is essential to find a near minimum value of N for a given accuracy goal.

How well does SSI work? We have demonstrated numerically in Figs. 4 and 5 the presence of exponential convergence. It is not that the gravitational wave fluxes fall geometrically (a known result), but that the gap between resolutions (i.e., error in substituting the DFT for the Fourier series) falls exponentially with increases in N. We can, however, go a step further and make the rate of exponential convergence even faster by introducing one final modification.

SSI is exponentially convergent because the periodic functions, $\bar{E}^{\pm}_{lmn}(t)$, being sampled are C^{∞}. However, there is no requirement that the periodic motion be described by t. Any C^{∞} reparametrization $t \to \lambda(t)$ should be expected to also give rapidly convergent sums. This is true, for example, in switching from t to the relativistic anomaly χ. We have found empirically, though, that use of χ as the curve parameter substantially improves the rate of exponential convergence.

To effect this change we rewrite Eqn. (3.22) with χ as the independent variable. Then the periodic motion is
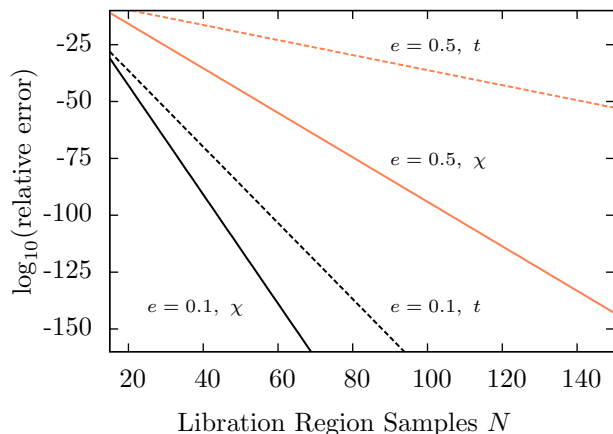
FIG. 6. Comparison between SSI with χ sampling and t sampling as a function of N and eccentricity. The two sampling schemes are tested by examining convergence of the $l = 2$, $m = 2$, $n = 0$ energy flux using the MST code. All orbits have $p = 10^3$.

divided into equally spaced steps $\Delta\chi = 2\pi/N$, the integrand is discretely sampled, and the integral is replaced with the sum

$$C_{lmn}^{\pm} = \frac{\Omega_r}{NW_{lmn}} \sum_k \frac{dt_p}{d\chi} \, \bar{E}_{lmn}^{\pm}[t(\chi_k)] \, e^{in\Omega_r t(\chi_k)}. \quad (3.31)$$

As Fig. 6 demonstrates, substantially fewer χ-samples are required than t-samples for SSI to reach a prescribed error level. This is especially true of high eccentricity orbits. As a practical matter, it is also easier to find φ_p and r_p evenly sampled in χ than in t. Finally, we comment that it was merely a hunch (though one informed by experience with the problem) that χ might provide a better measure and more rapid convergence. It is an open question whether there is another parametrization of the orbit that yields even faster convergence.

The numerical SSI results shown so far have involved the high accuracy MST code. But SSI also aids in double precision C coded calculations. Its benefit is shown clearly in Fig. 7, where we mark the accuracy reached in computing a normalization coefficient (C_{220}^+) as a function of the number of source term evaluations, which serves as a proxy for computational load. We compare SSI to an IVP ODE integration using an 8th order Runge-Kutta routine. SSI has exponentially converging accuracy with increases in function calls (i.e., increases in N). In contrast, the Runge-Kutta routine, with its algebraic convergence, struggles to reach high accuracies.

Do we really need SSI? The answer depends upon the application. At double precision the answer is clearly no, but SSI is likely much more efficient (and hence faster). The real critical requirement for SSI comes in high accuracy eccentric orbit calculations. Consider Fig. 7 again and the scaling of ODE integration. At an accuracy goal of 200 digits, even an efficient algorithm like 8th order

Runge-Kutta would take of order 10^{22} steps to integrate through an eccentric orbit source region! Without SSI or a comparable spectral method, these calculations simply cannot be done.

C. SSI and the midpoint and trapezoidal rules

We developed SSI with the convergence of Fourier series and concepts in signal processing (e.g., sampling theorem, use of the DFT/FFT, etc) firmly in mind. The application of SSI to orbit integration does in fact simply use the DCT, a special case of the DFT. In source integration, even though the key formula, (3.31) or (3.24), is not a DFT, we used the DFT to provide an understanding of the rapid convergence of the sum. The essential point was to see that rapid convergence in the FD with a modest number N of spectral elements could translate into representing the behavior in the TD with equally modest sampling. If the representation has sufficient accuracy, then interpolation and integration can be made accurately as well.

Yet, if we step back and examine the sums [(3.31) or (3.24)] that we use in SSI, a curious fact jumps out: they appear to be nothing more than simple Riemann sums. Given the sampling, their form appears to be a use of the left rectangle rule. However, with the inherent periodicity in χ, the left rectangle rule is equivalent to the trapezoidal rule and, with a half interval shift in the equal-sized χ bins, it is also just the midpoint rule. But these are just the lowest-order approximations for an integral, with error bounds, $\mathcal{O}(1/N^2)$, that are algebraic in the number of divisions of the interval! How can their use be giving a vastly faster rate of convergence? The answer lies in the periodicity and smoothness of the summands. After developing the method we came upon a paper [64] that discusses this surprising behavior in other contexts and nicely provides a set of example calculations. A more recent and exhaustive discussion is found in [65]. In black hole perturbation work, Fujita, Hikida, and Tagoshi [52] made use of the trapezoidal rule for source integration, but did not explicitly note or demonstrate the exponential convergence or push the results beyond double precision. The remarkably rapid convergence of the trapezoidal rule in special cases is apparently well known in certain numerical analysis circles, though it also appears to be something that is constantly being rediscovered ever since Poisson's original finding in 1827 [66].

Since we have shifted the viewpoint momentarily to thinking about Riemann sums and quadrature formulae, what about higher-order methods like Simpson's rule? Since Simpson's rule generally has a stronger error bound (implying presumably faster convergence) than the trapezoidal rule, might its use in SSI allow us to converge even faster? Alas, the answer is no, as a quick test demonstrated. A discussion and example can be found in [64].
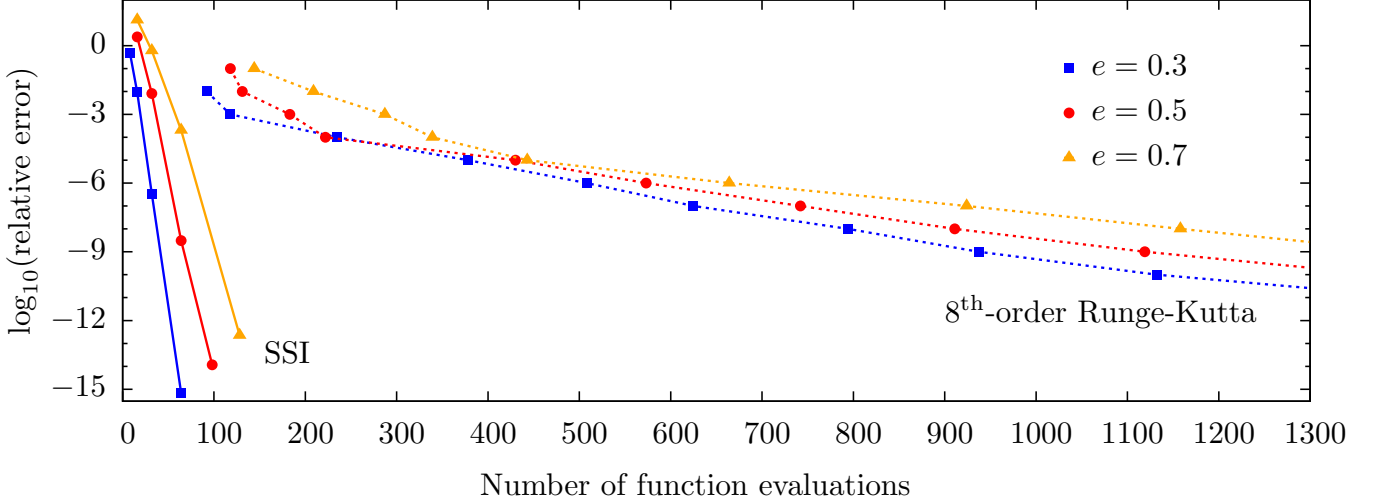
FIG. 7. Efficiency of spectral source integration in comparison to ODE integration in a RWZ application at double precision. The RWZ normalization constant C_{220}^+ is computed for various eccentricities in orbits with $p = 10$. The ODE integration uses the Runge-Kutta-Prince-Dormand 7(8) [62] routine rk8pd of the GNU Scientific Library (GSL) [63].

IV. SPECTRAL SOURCE INTEGRATION IN LORENZ GAUGE

After developing SSI for use in the RWZ formalism, we turned our attention to Lorenz gauge and were able to successfully apply the method to coupled systems of equations. Lorenz gauge breaks down into several systems of different orders that depend on (1) parity, (2) mode order (either low $l = 0, 1$ or high $l \geq 2$), and (3) the special static ($\omega = 0$) case. See [29] and [30] for details. Here we simply demonstrate the principles of incorporating SSI by focusing only on the odd-parity equations.

A. Odd-parity Lorenz gauge and EHS

In Lorenz gauge, odd-parity perturbations can be described by the two amplitudes, h_t^{lm} and h_r^{lm}, with the third, h_2^{lm}, obtainable from the gauge condition. The reduced-order coupled system in the TD is

$$\Box h_t^{lm} - \frac{2Mf}{r^2}\partial_r h_t^{lm} + \frac{2Mf}{r^2}\partial_t h_r^{lm} \qquad (4.1)$$
$$- \frac{2f^2 + (l+2)(l-1)f}{r^2}h_t^{lm} = f^2 P_{lm}^t,$$

$$\Box h_r^{lm} + \frac{2(r-M)f}{r^2}\partial_r h_r^{lm} - \frac{2(r-3M)}{r^2 f}\partial_t h_t^{lm} \qquad (4.2)$$
$$- \frac{2f^2 + (l+2)(l-1)f}{r^2}h_r^{lm} = -P_{lm}^r.$$

It is convenient in what follows to write the fields and their sources in a vector notation

$$\mathcal{B}_{lm}(t,r) = \begin{bmatrix} h_t^{lm} \\ f h_r^{lm} \end{bmatrix}, \quad \mathcal{V}_{lm}(t,r) = \begin{bmatrix} f^2 P_{lm}^t \\ -f P_{lm}^r \end{bmatrix}. \quad (4.3)$$

The Lorenz gauge source terms are proportional to the delta function $\delta[r - r_p(t)]$ (in contrast to RWZ gauge where the source also has a δ' term), allowing the source vector to be expressed in terms of a time-dependent vector amplitude $\boldsymbol{v}_{lm}(t)$,

$$\mathcal{V}_{lm}(t,r) \equiv \boldsymbol{v}_{lm}(t)\delta[r - r_p(t)]. \qquad (4.4)$$

The field $\mathcal{B}_{lm}$ and source $\mathcal{V}_{lm}$ can be expressed as Fourier series, analogous to Eqns. (3.3) and (3.4),

$$\mathcal{B}_{lm}(t,r) = \sum_{n=-\infty}^{\infty} \tilde{\mathcal{B}}_{lmn}(r)\, e^{-i\omega t}, \qquad (4.5)$$

$$\mathcal{V}_{lm}(t,r) = \sum_{n=-\infty}^{\infty} \tilde{\mathcal{V}}_{lmn}(r)\, e^{-i\omega t}. \qquad (4.6)$$

The FS coefficients are formally found via the integrals

$$\tilde{\mathcal{B}}_{lmn}(r) \equiv \frac{1}{T_r}\int_0^{T_r} dt\, \mathcal{B}_{lm}(t,r)\, e^{i\omega t}, \qquad (4.7)$$

$$\tilde{\mathcal{V}}_{lmn}(r) \equiv \frac{1}{T_r}\int_0^{T_r} dt\, \mathcal{V}_{lm}(t,r)\, e^{i\omega t}. \qquad (4.8)$$

With these definitions, we henceforth in this section suppress the TD mode labels lm and the FD labels lmn whenever no confusion might arise. However, for clarity we attach a tilde to denote FD quantities.

In the FD, the field equations (4.1) and (4.2) take the following form

$$\partial_{r_*}^2 \tilde{\mathcal{B}} + \mathbf{C}\,\partial_{r_*}\tilde{\mathcal{B}} + \mathbf{D}\,\tilde{\mathcal{B}} = \tilde{\mathcal{V}}. \qquad (4.9)$$

The matrices $\mathbf{C}$ and $\mathbf{D}$ that couple the equations are

given by

$$\mathbf{C} = \frac{2}{r^2} \begin{bmatrix} -M & 0 \\ 0 & r - 3M \end{bmatrix},$$

$$\mathbf{D} = \left(\omega^2 - \frac{2f^2 + (l+2)(l-1)f}{r^2} \right) \mathbb{I} \qquad (4.10)$$

$$+ \frac{2i\omega}{r^2} \begin{bmatrix} 0 & -M \\ r - 3M & 0 \end{bmatrix},$$

where $\mathbb{I}$ is the 2×2 identity matrix.

The EHS method carries over to Lorenz gauge [29, 30]. Four fundamental independent homogeneous solutions to Eqn. (4.9) are denoted by $\tilde{\boldsymbol{\mathcal{B}}}_i^{\pm}$, with $i = 0, 1$. The $\pm$ superscript delineates causal asymptotic behavior, with $+$ indicating an outgoing wave at $r_* = \infty$ and $-$ indicating a downgoing wave at $r_* = -\infty$. A Green function constructed from these arbitrarily normalized modes yields the solution to the inhomogeneous system

$$\tilde{\boldsymbol{\mathcal{B}}} = \tilde{\boldsymbol{\mathcal{B}}}_0^+ c_0^+ + \tilde{\boldsymbol{\mathcal{B}}}_1^+ c_1^+ + \tilde{\boldsymbol{\mathcal{B}}}_0^- c_0^- + \tilde{\boldsymbol{\mathcal{B}}}_1^- c_1^-, \qquad (4.11)$$

once the $c_i^{\pm}(r)$ are determined by integrating the first-order linear system

$$\mathbf{M}(r) \begin{bmatrix} \partial_{r_*} c_0^- \\ \partial_{r_*} c_1^- \\ \partial_{r_*} c_0^+ \\ \partial_{r_*} c_1^+ \end{bmatrix} = \begin{bmatrix} \mathbf{0} \\ \tilde{\boldsymbol{\mathcal{V}}}(r) \end{bmatrix}. \qquad (4.12)$$

Here $\mathbf{M}$ is the (lmn dependent) 4×4 Wronskian matrix

$$\mathbf{M}(r) \equiv \begin{bmatrix} \tilde{\boldsymbol{\mathcal{B}}}_0^- & \tilde{\boldsymbol{\mathcal{B}}}_1^- & \tilde{\boldsymbol{\mathcal{B}}}_0^+ & \tilde{\boldsymbol{\mathcal{B}}}_1^+ \\ \partial_{r_*} \tilde{\boldsymbol{\mathcal{B}}}_0^- & \partial_{r_*} \tilde{\boldsymbol{\mathcal{B}}}_1^- & \partial_{r_*} \tilde{\boldsymbol{\mathcal{B}}}_0^+ & \partial_{r_*} \tilde{\boldsymbol{\mathcal{B}}}_1^+ \end{bmatrix}, \qquad (4.13)$$

and $\mathbf{0}$ is the rank $= 2$ column vector.

Solving for the functions $c_i^{\pm}(r)$ can be avoided through use of the method of EHS. Instead, as in Sec. III, we solve for normalization coefficients, construct FD EHS and then TD EHS, and thus circumvent producing Gibbs behavior in the source region and at the particle location. For the system at hand, we define the normalization constants $C_i^{\pm}$ as

$$C_i^+ \equiv c_i^+(r_{\max}), \qquad C_i^- \equiv c_i^-(r_{\min}), \qquad (4.14)$$

and obtain them via the integrals

$$\begin{bmatrix} -C_0^- \\ -C_1^- \\ C_0^+ \\ C_1^+ \end{bmatrix} = \int_{r_{\min}}^{r_{\max}} \frac{1}{f(r)} \mathbf{M}(r)^{-1} \begin{bmatrix} \mathbf{0} \\ \tilde{\boldsymbol{\mathcal{V}}}(r) \end{bmatrix} dr. \qquad (4.15)$$

In the expression above, $\mathbf{M}(r)^{-1}$ is the inverse of the Wronskian matrix $\mathbf{M}(r)$. We next insert the integral expression for $\tilde{\boldsymbol{\mathcal{V}}}(r)$, reverse the order of integration, and

find the normalization coefficients with an integral over time,

$$\begin{bmatrix} -C_0^- \\ -C_1^- \\ C_0^+ \\ C_1^+ \end{bmatrix} = \frac{1}{T_r} \int_0^{T_r} \frac{1}{f_p} \mathbf{M}_p^{-1} \begin{bmatrix} \mathbf{0} \\ \boldsymbol{v}(t) \end{bmatrix} e^{i\omega t} dt. \qquad (4.16)$$

In this last equation the script p indicates time dependence via the mapping $r \to r_p(t)$. With the coefficients available, the FD and TD EHS (respectively) are constructed

$$\tilde{\boldsymbol{\mathcal{B}}}^{\pm}(r) \equiv C_0^{\pm} \tilde{\boldsymbol{\mathcal{B}}}_0^{\pm}(r) + C_1^{\pm} \tilde{\boldsymbol{\mathcal{B}}}_1^{\pm}(r), \qquad (4.17)$$

$$\boldsymbol{\mathcal{B}}^{\pm}(t, r) \equiv \sum_{n=-\infty}^{\infty} \tilde{\boldsymbol{\mathcal{B}}}^{\pm}(r) e^{-i\omega t}. \qquad (4.18)$$

The solution to the system in the TD, Eqns. (4.1) and (4.2), is then

$$\boldsymbol{\mathcal{B}}(t, r) = \boldsymbol{\mathcal{B}}^+ \theta \left[r - r_p(t) \right] + \boldsymbol{\mathcal{B}}^- \theta \left[r_p(t) - r \right]. \qquad (4.19)$$

The key to EHS in Lorenz gauge is solving systems like (4.16) for the normalization coefficients. In previous work [29, 30] these equations were treated as IVPs and solved with ODE integration. That numerical approach can be replaced with SSI to achieve spectral convergence, as we outline next.

B. Spectral source integration for odd-parity normalization constants

The Lorenz gauge employment of SSI is virtually identical to RWZ gauge. As in Eqn. (3.21), we can extract from the biperiodic source term $\boldsymbol{v}(t)$ the piece that is periodic in T_r by defining $\bar{\boldsymbol{v}}(t) \equiv \boldsymbol{v}(t) e^{im\Omega_\varphi t}$. Once substituted in Eqn. (4.16) we find

$$\begin{bmatrix} -C_0^- \\ -C_1^- \\ C_0^+ \\ C_1^+ \end{bmatrix} = \frac{1}{T_r} \int_0^{T_r} \bar{\boldsymbol{E}}(t) \, e^{in\Omega_r t} \, dt, \qquad (4.20)$$

where we define the vector

$$\bar{\boldsymbol{E}}(t) \equiv \frac{1}{f_p} \mathbf{M}_p^{-1} \begin{bmatrix} \mathbf{0} \\ \bar{\boldsymbol{v}}(t) \end{bmatrix}. \qquad (4.21)$$

Both $\bar{\boldsymbol{E}}(t)$ and $e^{in\Omega_r t}$ are periodic in T_r. The vector $\bar{\boldsymbol{E}}(t)$, which depends on the FD labels lmn, is the equivalent of $\bar{E}_{lmn}^{\pm}(t)$ in Eqn. (3.23).

The logical steps in implementing SSI carry over from Sec. III B:

- The vector $\bar{\boldsymbol{E}}(t)$ (carrying labels lmn) consists of periodic, C^{∞} functions.

- Each can be represented as a Fourier series with spectrum $\tilde{\boldsymbol{\mathcal{E}}}_{n'}$ with $n' \to \pm\infty$.

- The Fourier series spectrum can be truncated to some $n'_{\min} \le n' \le n'_{\max}$ subject to an accuracy goal.

- The approximate but very accurate truncated Fourier series is a bandlimited function.

- The Nyquist-Shannon sampling theorem implies the truncated Fourier series representation can itself be replaced in the TD with discrete sampling.

- Sampling plus periodicity implies a discrete representation of finite length N.

- Finite sampling representation in the TD implies one-to-one correspondence via the DFT with a FD periodic spectrum $\boldsymbol{\mathcal{E}}_{n'}$.

- The DFT spectrum within the first Nyquist minima approximates well the original Fourier series spectrum if N is sufficiently large, allowing $\tilde{\boldsymbol{\mathcal{E}}}_{n'} \to \boldsymbol{\mathcal{E}}_{n'}$.

Based upon this chain of reasoning, the integral (4.20) can be replaced with an exponentially convergent sum

$$\begin{bmatrix} -C_0^- \\ -C_1^- \\ C_0^+ \\ C_1^+ \end{bmatrix} = \frac{1}{N} \sum_{k=0}^{N-1} \bar{\boldsymbol{E}}(t_k)\, e^{in\Omega_r t_k}, \qquad (4.22)$$

where again $t_k = kT_r/N$. This is SSI for the systems of equations found in Lorenz gauge.

Even parity involves a larger linear system. The matrix inversion in evaluating $\bar{\boldsymbol{E}}(t_k)$ at the sample points is the most expensive task in double precision application. We use LU decomposition and take advantage of the symmetry $\mathbf{M}(t_k) = \mathbf{M}(T_r - t_k)$, so that LU decompositions of $\mathbf{M}$ are only necessary at $N/2 + 1$ points.

As in Sec. III B, we also attain a higher rate of exponential convergence by switching from t parametrization to χ. The adjustment to Eqn. (4.22) is straightforward

$$\begin{bmatrix} -C_0^- \\ -C_1^- \\ C_0^+ \\ C_1^+ \end{bmatrix} = \frac{\Omega_r}{N} \sum_{k=0}^{N-1} \frac{dt_p}{d\chi}\, \bar{\boldsymbol{E}}[t(\chi_k)]\, e^{in\Omega_r t(\chi_k)}, \quad (4.23)$$

where as before $\chi_k = 2\pi k/N$.

We have implemented SSI in just this way as a modification of the Lorenz gauge code described in Ref. [30]. SSI is particularly beneficial in Lorenz gauge, where a matrix must be inverted at each step (i.e., each function evaluation) in an integration. It is also beneficial that we know precisely where the sample locations are in the

source region before computing the inner and outer homogeneous solutions. The previous method found the normalization coefficients by integrating a large simultaneous system of ODEs through the source region (for the even-parity field this tallied to integrating 144 variables simultaneously). With prior knowledge of the sample locations, integration of the homogeneous solutions is decoupled from the SSI for the normalization coefficients.

As we described in Sec. III B, the number of sample points N is determined, iteratively if necessary, based on an error criterion. In all cases we have experience with, both RWZ and Lorenz gauge, it is the source integration (with SSI), not the spectral integration of the orbit, that sets the condition on N. In Lorenz gauge, the requirement on N to meet a double precision error criterion in SSI is about a factor of 8 larger than required for a comparably precise orbit integration. (With the MST code at a high accuracy of 200 digits, SSI requires an N that is about a factor of 2 larger than that required for comparably accurate orbit determination.) Because SSI shrinks so markedly the computational work in finding the normalization coefficients, our Lorenz gauge GSF code is sped up–overall–by a factor of about 3 for eccentricities of order $e \simeq 0.7$.

V. CONCLUSIONS

We have described in this paper a new method for achieving spectral accuracy and computational efficiency in calculating a broad class of black hole perturbation and gravitational self-force problems that entail generic orbital motion. This class should include most problems involving a point-particle description of the small compact object and use of the background geodesics in a frequency domain calculation (i.e., geodesic self-force calculations). We have shown it applied both to the RWZ formalism (for individual master equations) and to Lorenz gauge (with coupled systems of equations) for eccentric binaries with a Schwarzschild primary. The method should extend to extreme-mass-ratio inspirals on Kerr as well, which will be addressed in subsequent work. Called spectral source integration (SSI), this method provides an exponentially-convergent calculation of the mode normalization coefficients by replacing the more typically used ODE integrations in the source region. A simple modification of the underlying idea is also used to integrate the equations of orbital motion, to provide a consistent level of accuracy in determining source functions in the libration region.

Use of SSI in double precision calculations will improve code speed and help ensure optimal accuracy. In contrast, SSI is the *sine qua non* for calculating eccentric binaries using (MST) analytic function expansions at extraordinarily high accuracies (e.g., 200 decimal places). No algebraically convergent ODE solver will be able to calculate eccentric-orbit perturbations at hundreds of decimal places of accuracy. Any alternative to SSI will almost certainly be a similar technique using some other

spectral basis. A subsequent paper will describe use of SSI in an MST code to uncover new terms in the post-Newtonian expansion for eccentric binaries well beyond known 3PN order [45].

ACKNOWLEDGMENTS

Appendix A: Exact Fourier spectrum for $dt_p/d\chi$ as $p \to \infty$

Several figures in this paper have shown numerical evidence of exponential fall-off in the FD spectra of source functions in the perturbation and orbit equations. Here we demonstrate an exact calculation of the Fourier spectrum in one simplified case. Consider the source function $g(\chi)$ in Eqn. (2.5) and make a post-Newtonian expansion

$$\frac{dt_p}{d\chi} \equiv g(\chi) = \frac{Mp^{3/2}}{(1 + e \cos \chi)^2} + \mathcal{O}\left(p^{1/2}\right). \qquad (A1)$$

We then focus on the leading Newtonian term and seek to find its Fourier spectrum. Our derivation is similar to one found in [64]. Adopting the notation $g_N(\chi)$ for the term in question, we first introduce complex exponentials

$$g_N(\chi) = \frac{Mp^{3/2}}{\left[1 + \frac{1}{2}e\left(e^{i\chi} + e^{-i\chi}\right)\right]^2}. \qquad (A2)$$

The denominator in this expression can be factored

$$g_N(\chi) = \frac{4Mp^{3/2}\sigma^2}{e^2(1 + \sigma e^{i\chi})^2 \left(1 + \sigma e^{-i\chi}\right)^2}, \qquad (A3)$$

by introducing

$$\sigma = \frac{1}{e}\left(1 - \sqrt{1 - e^2}\right), \qquad (A4)$$

which is one of the roots of the quadratic equation $\sigma^2 - (2/e)\sigma + 1 = 0$. We then make a partial fractions decomposition of Eqn. (A3)

$$g_N(\chi) = \frac{Mp^{3/2}}{e^2(\sigma^2 - 1)^3}\left[4\left(1 + \sigma^2\right)\sigma^2 + \frac{4\sigma^2\left(\sigma^2 - 1\right)}{(1 + \sigma e^{i\chi})^2}\right.$$
$$\left. - \frac{8\sigma^4}{1 + \sigma e^{i\chi}} + \frac{4\sigma^2\left(\sigma^2 - 1\right)}{(1 + \sigma e^{-i\chi})^2} - \frac{8\sigma^4}{1 + \sigma e^{-i\chi}}\right]. \quad (A5)$$

Since it can be shown that $|\sigma| < 1$ for bound motion, each of the terms in Eqn. (A5) can be expanded in binomial or geometric series. The result is a Fourier series in χ. Because of the symmetry of $g_N(\chi)$, the expansion reduces to a cosine series

$$g_N(\chi) = \frac{1}{2}\mathcal{G}_0 + \sum_{n=1}^{\infty} \mathcal{G}_n \cos\left(n\chi\right), \qquad (A6)$$

and we find that the spectrum has the form

$$\mathcal{G}_n = \frac{8Mp^{3/2}(-1)^{n+1}}{e^2(1 - \sigma^2)^3}\left[(n - 1)\sigma^{n+4} - (n + 1)\sigma^{n+2}\right]. \qquad (A7)$$

The exponential convergence of the series is evident.

[1] A. Le Tiec, International Journal of Modern Physics D **23**, 1430022 (2014), arXiv:1408.5505 [gr-qc].

[2] T. W. Baumgarte and S. L. Shapiro, *Numerical Relativity: Solving Einstein's Equations on the Computer* (Cambridge University Press, 2010).

[3] L. Lehner and F. Pretorius, Annu. Rev. Astron. Astrophys. **52**, 661 (2014), arXiv:1405.4840 [astro-ph.HE].

[4] C. M. Will, Proceedings of the National Academy of Science **108**, 5938 (2011), arXiv:1102.5192 [gr-qc].

[5] L. Blanchet, Living Reviews in Relativity **17**, 2 (2014), arXiv:1310.1528 [gr-qc].

[6] S. Drasco and S. A. Hughes, Phys. Rev. D **69**, 044015 (2004).

[7] L. Barack, Class. Quant. Grav. **26**, 213001 (2009), arXiv:0908.1664 [gr-qc].

[8] E. Poisson, A. Pound, and I. Vega, Living Rev. Rel. **14**, 7 (2011), arXiv:gr-qc/1102.0529.

[9] J. Thornburg, GW Notes, Vol. 5, p. 3-53 **5**, 3 (2011), arXiv:1102.2857 [gr-qc].

[10] A. Buonanno and T. Damour, Phys. Rev. D **59**, 084006 (1999), gr-qc/9811091.

[11] A. Buonanno, Y. Pan, H. P. Pfeiffer, M. A. Scheel, L. T. Buchman, and L. E. Kidder, Phys. Rev. D **79**, 124028 (2009), arXiv:0902.0790 [gr-qc].

[12] T. Damour, Phys. Rev. D **81**, 024017 (2010), arXiv:0910.5533 [gr-qc].

[13] T. Hinderer, A. Buonanno, A. H. Mroué, D. A. Hemberger, G. Lovelace, H. P. Pfeiffer, L. E. Kidder, M. A. Scheel, B. Szilagyi, N. W. Taylor, and S. A. Teukolsky, Phys. Rev. D **88**, 084005 (2013), arXiv:1309.0544 [gr-qc].

[14] T. Damour, ArXiv e-prints (2013), arXiv:1312.3505 [gr-qc].

[15] A. Taracchini, A. Buonanno, Y. Pan, T. Hinderer, M. Boyle, D. A. Hemberger, L. E. Kidder, G. Lovelace, A. H. Mroué, H. P. Pfeiffer, M. A. Scheel, B. Szilágyi, N. W. Taylor, and A. Zenginoglu, Phys. Rev. D **89**, 061502 (2014), arXiv:1311.2544 [gr-qc].

[16] Y. Mino, M. Sasaki, and T. Tanaka, Phys. Rev. D **55**, 3457 (1997).

[17] T. C. Quinn and R. M. Wald, Phys. Rev. D **56**, 3381 (1997).

[18] P. Amaro-Seoane, J. R. Gair, A. Pound, S. A. Hughes, and C. F. Sopuerta, ArXiv e-prints (2014), arXiv:1410.0958.

[19] D. A. Brown, J. Brink, H. Fang, J. R. Gair, C. Li, G. Lovelace, I. Mandel, and K. S. Thorne, Physical Review Letters **99**, 201102 (2007), gr-qc/0612060.

[20] P. Amaro-Seoane, J. R. Gair, M. Freitag, M. C. Miller, I. Mandel, C. J. Cutler, and S. Babak, Class. Quant. Grav. **24**, R113 (2007), arXiv:astro-ph/0703495.

[21] L. Barack and A. Ori, Phys. Rev. D **61**, 061502 (2000), arXiv:gr-qc/9912010.

[22] K. Martel, Phys. Rev. D **69**, 044025 (2004).

[23] L. Barack and N. Sago, Phys. Rev. D **75**, 064021 (2007), arXiv:gr-qc/0701069.

[24] S. E. Field, J. S. Hesthaven, and S. R. Lau, Class. Quant. Grav. **26**, 165010 (2009), arXiv:0902.1287 [gr-qc].

[25] P. Canizares and C. F. Sopuerta, ArXiv e-prints (2014), arXiv:1406.7154 [gr-qc].

[26] S. Detweiler, Phys. Rev. D **77**, 124026 (2008), arXiv:0804.3529 [gr-qc].

[27] S. Hopper and C. R. Evans, Phys. Rev. D **82**, 084010 (2010).

[28] S. Akcay, Phys. Rev. D **83**, 124026 (2011).

[29] S. Akcay, N. Warburton, and L. Barack, Phys. Rev. D **88**, 104009 (2013), arXiv:1308.5223 [gr-qc].

[30] T. Osburn, E. Forseth, C. R. Evans, and S. Hopper, Phys. Rev. D **90**, 104031 (2014).

[31] I. Vega and S. Detweiler, Phys. Rev. D **77**, 084008 (2008), arXiv:0712.4405 [gr-qc].

[32] I. Vega, B. Wardell, and P. Diener, Classical and Quantum Gravity **28**, 134010 (2011), arXiv:1101.2925 [gr-qc].

[33] B. Wardell, I. Vega, J. Thornburg, and P. Diener, Phys. Rev. D **85**, 104044 (2012), arXiv:1112.6355 [gr-qc].

[34] M. Casals, S. Dolan, A. C. Ottewill, and B. Wardell, Phys. Rev. D **79**, 124043 (2009), arXiv:0903.0395 [gr-qc].

[35] M. Casals, S. Dolan, A. C. Ottewill, and B. Wardell, Phys. Rev. D **88**, 044022 (2013), arXiv:1306.0884 [gr-qc].

[36] B. Wardell, C. R. Galley, A. Zenginoğlu, M. Casals, S. R. Dolan, and A. C. Ottewill, Phys. Rev. D **89**, 084021 (2014), arXiv:1401.1506 [gr-qc].

[37] N. Sago, L. Barack, and S. L. Detweiler, Phys. Rev. D **78**, 124024 (2008), arXiv:0810.2530 [gr-qc].

[38] L. Blanchet, S. Detweiler, A. Le Tiec, and B. F. Whiting, Phys. Rev. D **81**, 064004 (2010), arXiv:0910.0207 [gr-qc].

[39] L. Blanchet, S. Detweiler, A. Le Tiec, and B. F. Whiting, Phys. Rev. D **81**, 084033 (2010), arXiv:1002.0726 [gr-qc].

[40] R. Fujita, Progress of Theoretical Physics **128**, 971 (2012), arXiv:1211.5535 [gr-qc].

[41] A. G. Shah, J. L. Friedman, and B. F. Whiting, Phys. Rev. D **89**, 064042 (2014), arXiv:1312.1952 [gr-qc].

[42] A. G. Shah, Phys. Rev. D **90**, 044025 (2014), arXiv:1403.2697 [gr-qc].

[43] A. G. Shah and A. Pound, (2015), arXiv:1503.02414 [gr-qc].

[44] S. Mano, H. Suzuki, and E. Takasugi, Progress of Theoretical Physics **95**, 1079 (1996), gr-qc/9603020.

[45] E. Forseth, C. R. Evans, and S. Hopper, (in preparation, 2015).

[46] C. Hopman and T. Alexander, Astrophysical Journal **629**, 362 (2005), arXiv:astro-ph/0503672.

[47] B. Moore, M. Favata, K. Arun, and C. Mishra (2015), Talk presented at the APS April meeting held in Baltimore, MD, `http://meetings.aps.org/Meeting/APR15/Session/R13.1`.

[48] C. Cutler, D. Kennefick, and E. Poisson, Phys. Rev. D **50**, 3816 (1994).

[49] L. Barack, A. Ori, and N. Sago, Phys. Rev. D **78**, 084021 (2008), arXiv:0808.2315.

[50] N. Warburton and L. Barack, Phys. Rev. D **83**, 124038 (2011), arXiv:1103.0287 [gr-qc].

[51] S. Drasco and S. A. Hughes, Phys. Rev. D **73**, 024027 (2006), gr-qc/0509101.

[52] R. Fujita, W. Hikida, and H. Tagoshi, Prog. Theor. Phys. **121**, 843 (2009), arXiv:0904.3810 [gr-qc].

[53] L. Barack and N. Sago, Phys. Rev. D **81**, 084021 (2010), arXiv:1002.2386 [gr-qc].

[54] C. Darwin, Proceedings of the Royal Society of London. Series A: Mathematical and Physical Sciences **263**, 39 (1961).

[55] I. S. Gradshteyn, I. M. Ryzhik, A. Jeffrey, and D. Zwillinger, *Table of Integrals, Series, and Products, Seventh Edition by I. S. Gradshteyn, I. M. Ryzhik, Alan Jeffrey, and Daniel Zwillinger. Elsevier Academic Press, 2007. ISBN 012-373637-4* (2007).

[56] W. H. Press, S. A. Teukolsky, W. T. Vetterling, and B. P. Flannery, *Numerical Recipes in C: The Art of Scientific Computing*, 2nd ed. (Cambridge University Press, Cambridge, UK, 1993).

[57] R. Fujita and W. Hikida, Classical and Quantum Gravity **26**, 135002 (2009), arXiv:0906.1420 [gr-qc].

[58] F. Stenger, SIAM Review **23**, pp. 165 (1981).

[59] N. Ahmed, T. Natarajan, and K. R. Rao, IEEE Trans. Comput. **23**, 90 (1974).

[60] K. R. Rao and P. Yip, *Discrete Cosine Transform: Algorithms, Advantages, Applications* (Academic Press Professional, Inc., San Diego, CA, USA, 1990).

[61] M. Sasaki and H. Tagoshi, Living Reviews in Relativity **6**, 6 (2003), gr-qc/0306120.

[62] P. Prince and J. Dormand, Journal of Computational and Applied Mathematics **7**, 67 (1981).

[63] "Gnu scientific library," `http://www.gnu.org/software/gsl/`.

[64] J. A. C. Weideman, American Mathematical Monthly **109**, 21 (2002).

[65] L. N. Trefethen and J. Weideman, SIAM Review **56**, 385 (2014).

[66] S. D. Poisson, Memoires de l'Academie Royale des Sciences de l'Institut de France **4**, 571 (1827), `http://hdl.handle.net/2027/mdp.39015077785494?urlappend=%3Bseq=769`.